Materials Characterization 199 (2023) 112815

Contents lists available at ScienceDirect

Materials Characterization

journal homepage: www.elsevier.com/locate/matchar

Plastic inhomogeneity and crack initiation in hybrid wrought - additively manufactured Inconel 718

Jalal Al-Lami [a,*], Phuc Hoang [a], Catrin Davies [b], Talha Pirzada [c], Minh-Son Pham [a]

[a] Department of Materials, Imperial College London, London, UK
[b] Department of Mechanical Engineering, Imperial College London, London, UK
[c] Department of Materials, University of Oxford, Oxford, UK

ARTICLE INFO

Keywords:
Additive manufacturing
Directed energy deposition
Hybrid manufacturing
Inconel 718
Plastic deformation
Plastic inhomogeneity
Strain localisation
Work hardening

ABSTRACT

Directed energy deposition (DED) holds great promise for repair applications involving site-specific deposition that creates hybrid components. However, it has been reported that failure in hybrid components occurs in the additively manufactured (AM) side despite its higher strength and excellent consolidation. To unravel the underlying mechanisms responsible for the observed behaviour, we carried out both *ex-situ* and *in-situ* mechanical testing complemented with detailed microstructural characterisation of the wrought, AM and bond interface regions in hybrid Inconel 718. The role of the local microstructure in the spatial strain development and crack initiation in the hybrid wrought-AM Inconel 718 is revealed. Most importantly, it is shown that severe inhomogeneous plastic deformation quickly developed in the AM side of the hybrid sample, and this is primarily attributed to few, but very large columnar grains that were preferentially oriented for dislocation slip under external loading. Furthermore, the AM region of the hybrid Inconel 718 had a lower work-hardening rate that caused a higher thinning rate during deformation, promoting strain localisation in the AM side. The degradation in the ductility of AM Inconel 718 is shown to have occurred not because of defects as widely reported for AM components, but rather as a consequence of the interaction between the brittle Laves phase with the localised slip bands which were rapidly intensified by the plastic inhomogeneity. This interaction resulted in early crack initiation in the AM side, primarily leading to the final fracture of the hybrid wrought-AM Inconel 718. The study also demonstrates that the bond interface is the strongest region of the hybrid component under uniaxial loading, and reveals the origins of the strength of the bond interface. The insights revealed advance the understanding of the mechanical performance and the direct failure mechanism in hybrid wrought-AM Inconel 718 components, and opens new pathways to improve their mechanical integrity.

1. Introduction

Directed energy deposition (DED) is an effective additive manufacturing (AM) and repair technology. DED has multiple advantages over other processes. For example, the printing process in DED is not confined by a build chamber size as in other AM processes [1]. Also, the typical heat affected zone (HAZ) and distortion that result from welding processes and compromise the component integrity are substantially less severe in DED [2,3]. Yu *et al.* [4] concluded that the heat affected zone is 21 times smaller using DED in comparison with arc welding. The benefits offered by DED have resulted in its wide use for manufacturing components [5], in repair applications involving site-specific deposition [2,6], and for manufacturing hybrid components [7,8]. The DED process involves a high local heat input coupled with rapid cooling rates that vary with respect to the location in the build [9]. This creates a spatial variation of thermal gradient leading to a microstructural gradient across the AM build, which is particularly pronounced in the vicinity of the bond interface between the AM build and substrate [8,10,11]. In addition, the distinctive differences in microstructure between the AM and substrate regions in hybrid (or repaired) components cause significant plastic inhomogeneity of the components under mechanical loading. It is known that plastic inhomogeneity is responsible for the strain localisation and subsequent failure of metallic alloys. Therefore, an in-depth understanding of the plastic inhomogeneity in the three regions (namely the bond interface, AM and substrate regions) is crucial to reveal the failure mechanism, helping to

* Corresponding author.
E-mail address: j.al-lami18@imperial.ac.uk (J. Al-Lami).

https://doi.org/10.1016/j.matchar.2023.112815
Received 9 September 2022; Received in revised form 18 February 2023; Accepted 10 March 2023
Available online 13 March 2023

ensure the mechanical integrity and the overall performance of DED builds.

A significant number of studies have been performed to investigate the microstructure and mechanical properties of DED builds, in particular for the model alloy Inconel 718 [2,7,8,10,12–14]. Inconel 718 is one of the most commonly utilised alloys in high-temperature applications, owing to its high strength and excellent resistance to creep, fatigue and corrosion up to 700 °C [15]. Guévenoux *et al.* [10] studied the influence of the microstructural gradient of the bond interface neighbourhood on the plastic strain localisation in an Inconel 718 wrought substrate repaired by DED. The study showed that strain localisation and fracture occurred in the AM region [10]. In a similar study performed on DED-repaired 316L stainless steel, Balit *et al.* [16] reported that, despite having a higher strength than the substrate, the AM region was the one in which inhomogeneous deformation, strain localisation and fracture occurred. Although this was attributed to the grain size effect, the strain localisation is not only influenced by the grain size but also the crystallographic orientation distribution and the spatial distribution of other microstructure such as the dislocation density, chemical segregation and secondary particles.

Despite the important observation showing the localisation and crack initiation in the AM side, there has been limited understanding of the mechanisms governing the inhomogeneity of plastic deformation. Most importantly, there has not been an examination on how the interaction of localisation (as a result of the plastic inhomogeneity) and other local microstructure (such as Laves phase) affects the crack initiation in hybrid wrought-AM Inconel 718. Such examination will help to understand the loss in ductility of hybrid wrought-AM builds due to characteristic AM microstructure. Even though Inconel 718 components are typically heat treated when used in practice, it is crucial to study the link between the spatial deformation behaviour and individual microstructural features in as-built, non-heat treated hybrid Inconel 718 because it helps to understand what microstructural features are most detrimental (or beneficial) for the development of localisation and subsequent damage. This essential understanding would guide towards the *in-situ* microstructure engineering by AM processing, and provide better knowledge in selecting more appropriate heat treatment conditions to optimise the AM microstructure, in particular retaining the beneficial microstructural features and eliminating the undesired ones. Therefore, this study firstly carried out a comprehensive examination of the grain morphology, dislocation density, dendritic arm spacing, chemical segregation, and crystallographic orientation to study the mechanical constitutive behaviour and plastic inhomogeneity in an as-built hybrid condition consisting of the bond interface, AM deposit and wrought condition. Secondly, the evolution of plastic inhomogeneity and the interaction between the strain localisation and other microstructure were investigated using *ex-situ* and *in-situ* mechanical testing to study the role of the plastic inhomogeneity and Laves phase in the crack initiation, helping to reveal the underlying mechanisms responsible for the loss in ductility of Inconel 718.

2. Material and methods

2.1. Hybrid wrought-AM manufacturing

A hybrid block was manufactured by the DED deposition of Inconel 718 on a substrate of wrought Inconel 718. A Trumpf DMD 505 machine with a CO_2 laser was used to deposit a block of dimensions 100 mm (L) x 40 mm (W) x 50 mm (D) on the substrate. The substrate was an annealed block of dimensions 200 mm (L) x 45 mm (W) x 50 mm (D). Fresh plasma atomised powder sourced from AP&C was used and the AM process was performed at TWI, Sheffield using optimised processing parameters. DED was performed in a bi-directional raster scan strategy at a deposition rate of 0.2 kg/h, laser power 1050 W and scan speed 11.25 mm/s. The volumetric energy density was calculated to be 159.5 J/mm^3.

2.2. Mechanical testing

Wire electrical discharge machining (EDM) was used to extract different sample profiles (Fig. 1) from the hybrid block for microstructural characterisation and mechanical testing. In addition to machining hybrid samples, individual AM and wrought samples were extracted. The axis of all machined samples was parallel to the building direction, and the bond interface between the DED deposit and the substrate was located at the centre of the gauge of each hybrid sample.

An Instron machine was used for tensile testing the hybrid samples, Fig. 1a, at a strain rate of 10^{-3} s^{-1}. The strain was measured by digital image correlation (DIC) using a high-resolution camera. In preparation for DIC tensile testing, the samples were ground, polished and spray painted with a white primer followed by matte black paint to create a speckle pattern. During loading, images of 4000 × 3000 pixel resolution were captured at a rate of 2 images per second for DIC processing, which was performed using GOM Correlate software. Non-contact strain quantification by DIC enabled full-field strain measurement across the gauge of the samples. In addition, virtual extensometers were added across the full length of the gauge region as well as across the constituent wrought and AM sides in the hybrid samples to study their local deformation behaviour under uniaxial loading.

The DIC tensile testing setup of the hybrid samples was also adopted for tensile testing samples of either only the wrought or AM condition, Fig. 1b. Understanding the behaviour of the two individual conditions was important to study their interaction and influence on the tensile behaviour of the hybrid Inconel 718 containing both the wrought and AM components.

To assess the influence of the microstructural gradient near the bond interface on the local microhardness, Vickers microhardness testing was performed. Indentations at a step of 300 μm were made from the interface towards the bulk of the AM and wrought sides. In addition, microhardness measurements were performed along the bond interface and along lines in the wrought and AM sides that were parallel to the interface but 5 mm distant from it. At least 10 indentations were performed for each measurement set while maintaining a distance between the indentations of around three times the diagonal length of the indented region.

2.3. Microstructural characterisation

In preparation for microscopy work, samples were first ground with SiC paper in sequential steps using 800, 1200, 2000 and 4000 P-grades. This was followed with polishing using a 50%–50% mixture of oxide polishing suspension (OPS) diluted in distilled water. Samples were examined in unetched and etched conditions. Etching was performed by applying Aqua Regia (5mm^3 HNO_3 freshly mixed with 15mm^3 HCl) on the polished surface for 7–10 s.

Microstructural characterisation was performed using the Olympus BX53M optical microscope, Zeiss Auriga scanning electron microscope (SEM), and Zeiss Sigma 300 SEM equipped with an energy dispersive X-ray spectroscopy (EDS) detector and a high-resolution electron backscatter diffraction (EBSD) detector. SEM imaging was performed in secondary electron (SE) and backscattered electron (BSE) modes using a voltage of 15 kV. EBSD and EDS were performed simultaneously using a voltage of 20 kV, aperture of 120 μm, and step size of 1 μm. The EDS data was processed using Esprit software and the EBSD data was processed using both Esprit software and MTEX in MATLAB. The density and spatial distribution of GNDs were calculated from the EBSD data using MTEX. The GND calculation from EBSD data is based on the quantification of crystallographic orientation variations. The local orientation difference between neighbouring points in a grain is used to derive the lattice curvature tensor and the dislocation density tensor. Calculated GNDs are the minimum necessary density to accommodate the local orientation gradients to ensure lattice continuity [17,18]. The detailed mathematical description on which the MTEX code is based can be

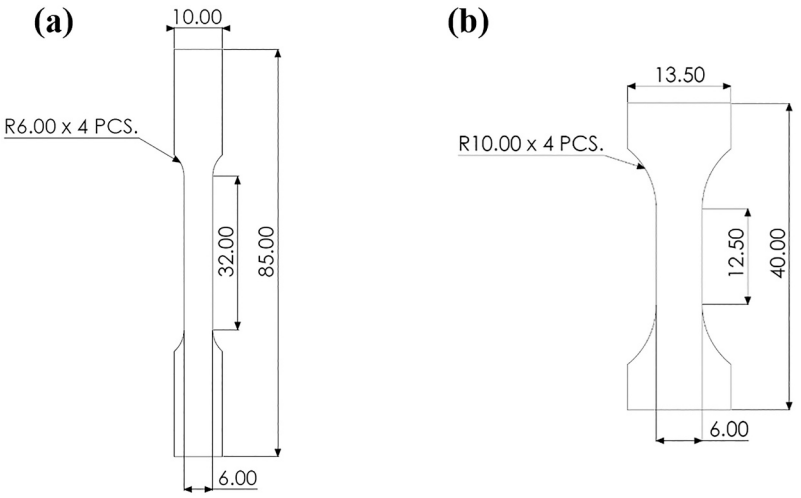

Fig. 1. Tensile testing samples: (a) hybrid sample with a thickness of 2 mm; (b) sample of either only the wrought or AM condition with a thickness of 2 mm. All dimensions are in mm and figures not to scale.

found in Pantleon's study [19].

3. Results and discussion

3.1. Microstructure in the bond interface region

The local microstructure in each of the wrought, AM and bond interface regions of the hybrid Inconel 718 is first presented in sections 3.1 and 3.3. Afterwards, the mechanisms governing the plastic inhomogeneity and crack initiation in hybrid Inconel 718 are revealed and discussed in sections 3.4 and 3.5 in light of the presented microstructure.

Fig. 2 shows the microstructure of the AM, bond interface and wrought regions of the hybrid Inconel 718. High consolidation and absence of defects, in particular at the interface region, are important for the mechanical integrity of hybrid components. Microscopy imaging revealed that the hybrid component had an excellent consolidation of 99.97% with observation of no lack of fusion, not only in the vicinity of the bond interface but also in the bulk of the AM deposit.

The cellular dendritic microstructure is influential in the mechanical behaviour of AM alloys, including Inconel 718 [20–22]. The microstructure was observed in the AM side and the primary dendrite arm spacing (PDAS) was experimentally measured in relation to distance from the interface, Fig. 3a. Owing to the cellular dendritic growth, secondary dendrite arms did not sufficiently develop to be considered, hence only the PDAS was measured and reported. The PDAS was found to increase with distance from the interface in agreement with previous studies [9,23]. This change in PDAS is caused by a reduction in the local cooling rate towards the top of AM builds. The heat transfer primarily occurs via conduction through the previously deposited layers and substrate underneath. Therefore, as more DED layers were deposited, the thermal build-up increased and the local cooling rate decreased, resulting in an increase in PDAS. The local cooling rate at a given location is proportional to the PDAS measured as follows [21,23–27]:

$$\lambda = 80\dot{T}^{-0.33} \quad (1)$$

where λ is the PDAS in μm and $\dot{T}$ is the cooling rate in K/s. Fig. 3b shows the variation in the cooling rate (estimated using Eq. (1)) with the change in the measured PDAS.

The crystallographic orientations of grains in the bond interface region with respect to the building direction (BD) in the hybrid sample are displayed in Fig. 4a. The microstructure in the AM side next to the interface is dominated by small grains of rather randomly crystallographic orientations. However, as the distance from the interface increased, there was competition between the growth of different crystallographically-oriented grains. Grains that were more aligned with the thermal gradient outgrew other misaligned grains [28]. Competitive growth between grains led to the coarsening of preferred grains in the AM microstructure, resulting in an increase in grain size with distance

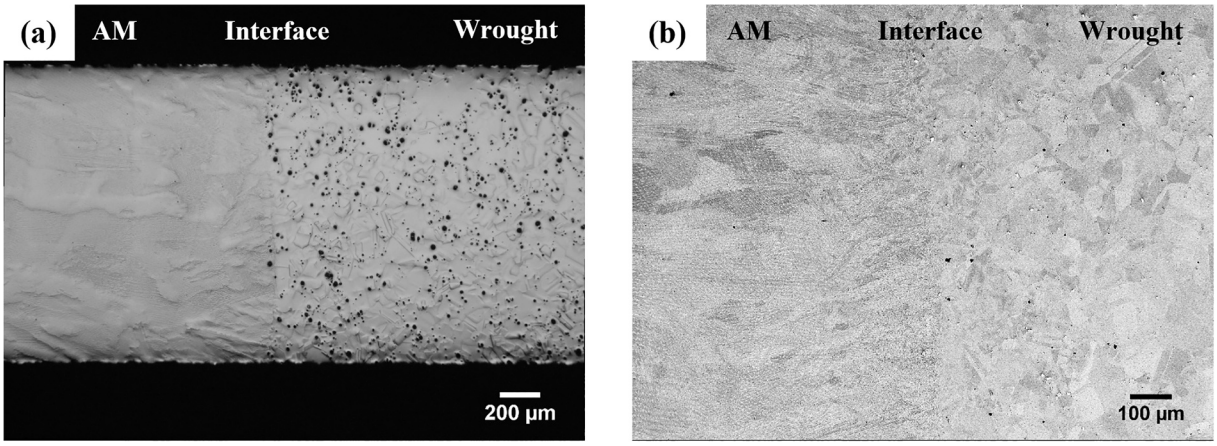

Fig. 2. Interface linking the AM deposit with the wrought material in the hybrid sample: (a) optical micrograph; (b) SEM image. Note that the dark features in the wrought side seen in the optical micrograph in (a) were carbides and not pores.

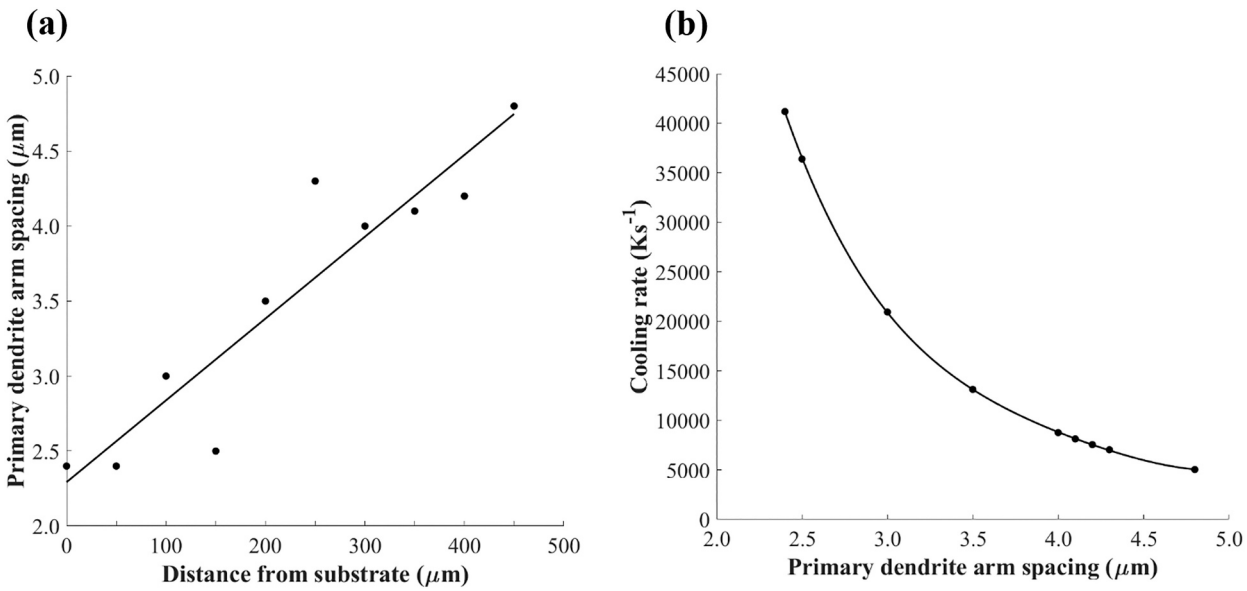

Fig. 3. (a) The variation of the experimentally measured PDAS with distance from the bond interface; (b) estimated cooling rate in relation to the measured PDAS.

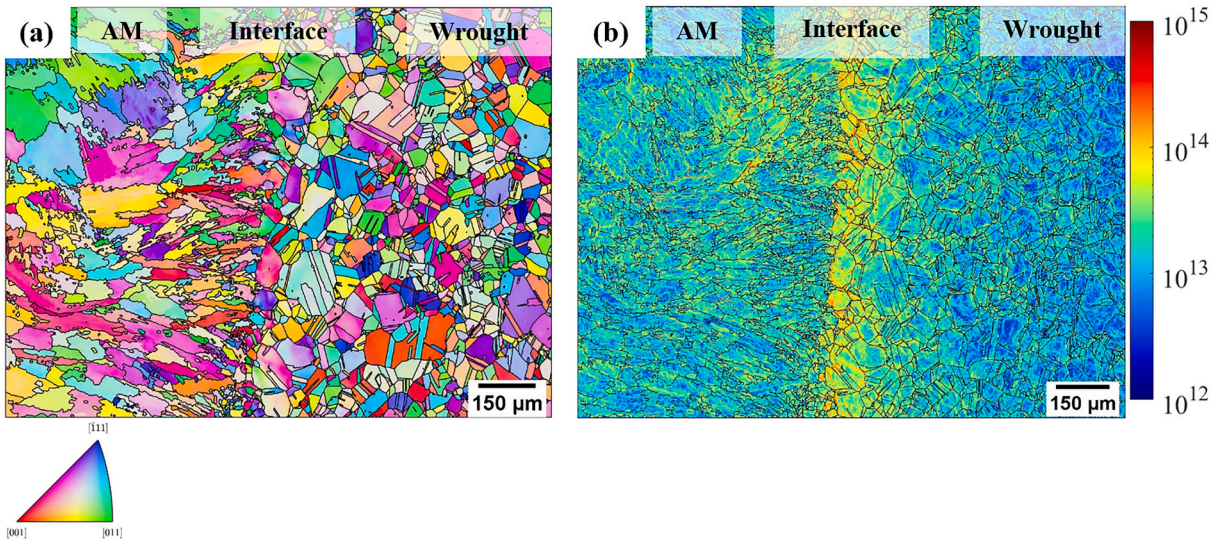

Fig. 4. Microstructure in the bond interface region: (a) inverse pole figure (IPF)-BD map showing the variation in grain size and crystallographic orientation at the interface region; (b) estimate of GND spatial distribution of the same area shown in (a). Note: the unit of the scale bar is m^{-2}.

from the bond interface.

On the other side of the interface, grains in the wrought substrate were equiaxed. The grains in the HAZ near the interface were larger in size in comparison to those in the bulk region of the wrought side, as detailed in Table 1. Also, the grains adjacent to the interface contained a high density of geometrically necessary dislocations (GNDs), as shown in Fig. 4b, which resulted from the high thermal gradient in the wrought substrate. It is worth mentioning that although the GND measurement by EBSD provides significant insights into the accumulation and spatial distribution of dislocations, it does not provide information on statistically stored dislocations (SSDs) which also contribute to strain hardening. While the generation and pile-up of dislocations increases the local strength at the interface region of the hybrid component, it reduces the local ductility.

Table 1
Average grain size measured from EBSD maps with respect to distance from the bond interface.

	Wrought region			AM region		
	100 μm from interface	500 μm from interface	5000 μm from interface	100 μm from interface	500 μm from interface	5000 μm from interface
Average grain size (μm)	81	63	23	106	156	902

3.2. Microstructure in the wrought and AM regions

An EBSD IPF-BD map of the AM region presented in Fig. 5a shows that competitive growth led to the development of mm-large, columnar grains. The colour gradient within individual grains in the IPF-BD map indicates slight misorientations due to the change in orientation across the interdendritic regions within individual grains, Fig. 5c. Fig. 6 reveals that the GNDs located at the interdendritic boundaries partly accommodate the misorientation between dendrites. The dense presence of GNDs in interdendritic regions is consistent with TEM observations reported in other studies on Inconel 718 fabricated by laser powder-bed fusion (L-PBF) showing the high initial dislocation density accumulated at the cellular (or dendritic) boundaries [21,29]. The accumulation of dislocations can increase the critical resolved shear stress for

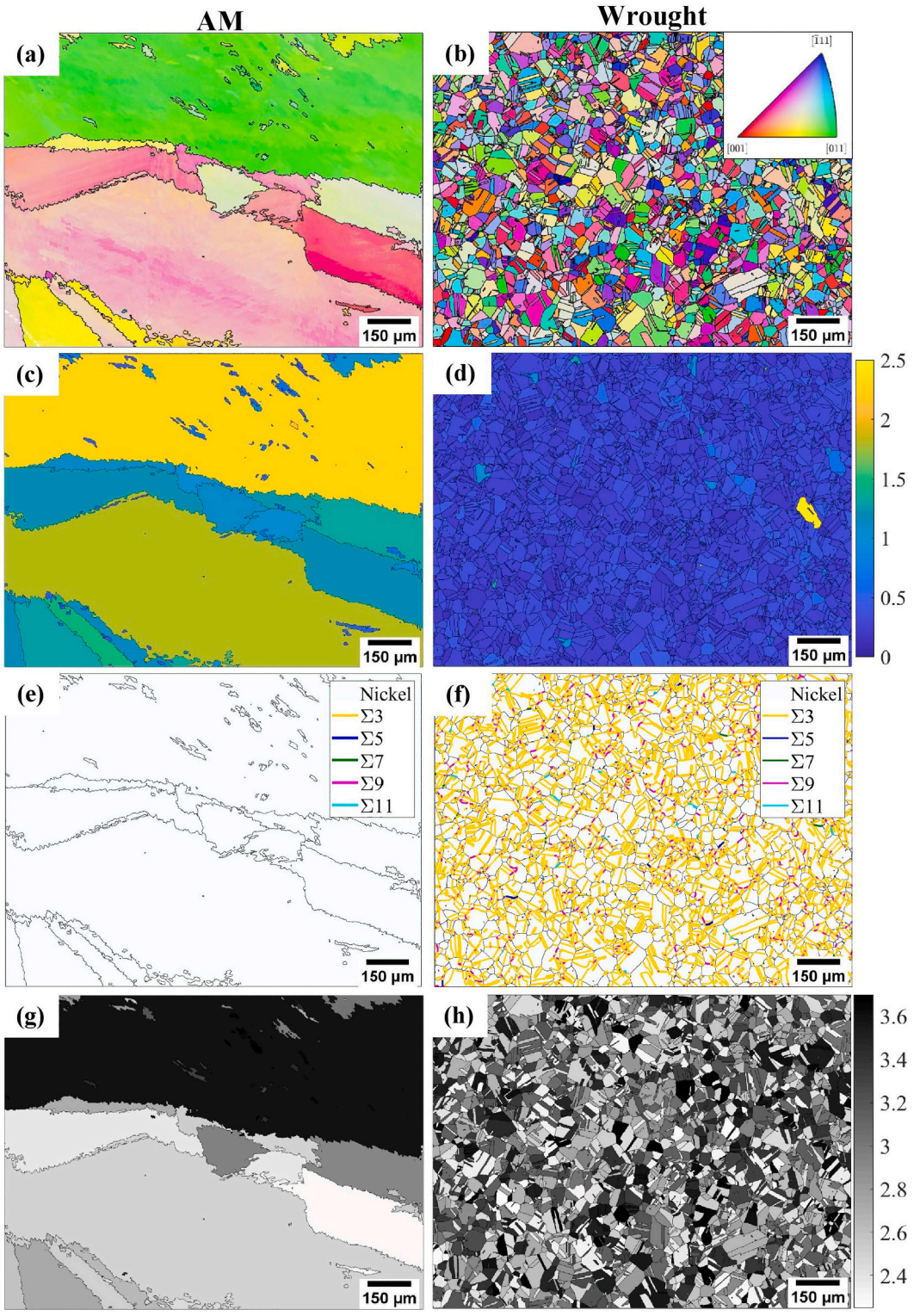

Fig. 5. Microstructure in the bulk AM and wrought regions in the hybrid sample: (a) and (b) IPF-BD figures; (c) and (d) grain orientation spread (GOS) maps; (e) and (f) twin boundary maps; (g) and (h) Taylor factor maps. Note: AM condition was shown in the left column while the wrought was in the right column.

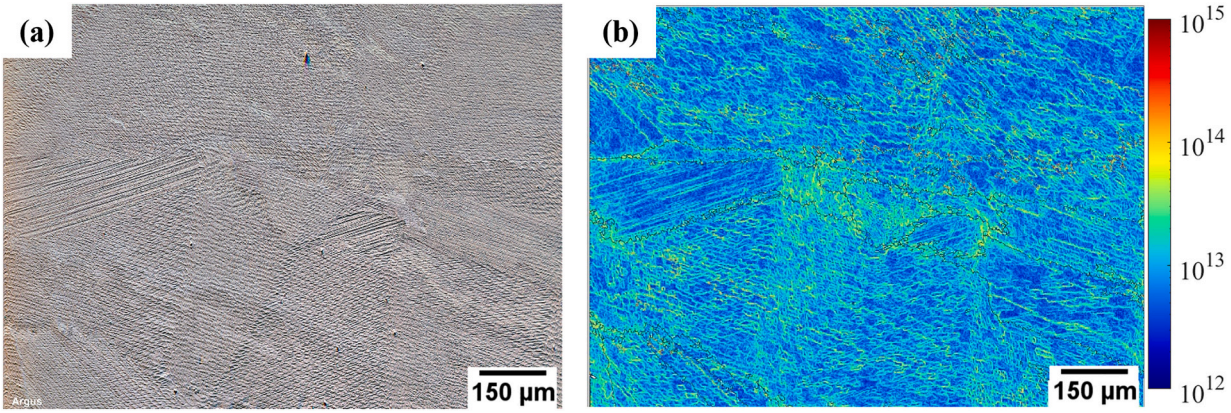

Fig. 6. (a) SEM micrograph showing cellular dendritic growth in the AM microstructure; (b) EBSD-GND spatial distribution map of the same area shown in (a), measured in m^{-2}.

dislocations to slip, leading to high initial yield stress.

In the wrought region far from the interface, the grains were equiaxed and substantially smaller than those in the AM region, Fig. 5b. Also, lots of annealing Σ3 twin boundaries were detected in the region. In fact, the Σ3 boundaries constituted 89% of the grain boundaries, but this is not surprising because the wrought substrate was annealed. In contrast, no Σ3 twin boundaries were detected in the AM material.

Deformation of most polycrystalline metals including Inconel 718 occurs by dislocation slip. The slip response in each grain depends on the crystallographic orientation of the grain with respect to the imposed stress state. The Taylor factor reflects the influence of the crystallographic orientation of grains on their slip activity. The higher the Taylor factor, the lower the slip activity. A higher number of slip systems can be activated in individual grains of lower Taylor factors that are more favourably oriented with respect to the applied stress state in comparison with other grains that are not preferably oriented. The Taylor factor maps shown in Fig. 5g-h reveal that the wrought region contained a random distribution of relatively small "soft" and "hard" grains (i.e. grains with low and high Taylor factors, respectively). However, the AM region contained significantly larger grains, with dominant ⟨100⟩ and ⟨110⟩ orientations along the build direction. As shown in Fig. 5g, the ⟨110⟩ oriented grains had higher Taylor factors and were "harder" and more resistant to plastic deformation under uniaxial loading along the building direction.

3.3. Chemical characterisation

In the wrought region, precipitates had an area fraction of 0.54% and an average size of 5.3 μm. EDS analysis was performed to identify these precipitates, as detailed in Table 2. The chemical composition shows that the precipitates were rich in Nb, Ti and C elements but depleted in Ni, Fe and Cr, suggesting they were likely to be (Nb,Ti)C carbides.

Fig. 7 demonstrates clear elemental segregation towards interdendritic regions in the AM side, with notable Nb segregation, in agreement with previous studies reported on Inconel 718 fabricated by additive manufacturing [21,30–32].

Fine precipitates were also observed in the interdendritic regions in the AM microstructure, as shown in Fig. 8. These precipitates are widely reported in literature [8,9,12,33–35] as the Laves phase $(Ni,Fe,Cr)_2(Nb,Mo,Ti)$. Laves phase is usually considered undesirable because of its brittle nature [8,15,35]. The size and morphology of Laves phase are influenced by the processing parameters used during the DED process. Studies suggest that using a lower energy input during DED increases the cooling rate, which in turn results in a refined microstructure with smaller Laves phase [33,34]. As the energy input and deposition rate used in this study were relatively low, the precipitated Laves phase was small. However, the area fraction of the Laves phase decreased from around 2.3% in the AM region near the bond interface to 1.0% in the bulk region. Moreover, atom probe tomography investigations reported by Piglione *et al.* [21] indicate that very fine carbides were also seen within or in the vicinity of the Laves phase.

3.4. Plastic inhomogeneity in wrought-AM hybrid condition

3.4.1. Plasticity and localisation in the hybrid condition

While the previous sections report the distinct microstructure in each of the wrought, AM and bond interface regions of the hybrid component, this section reveals the direct role of the local microstructure in the spatial strain development and mechanical responses. The tensile properties are presented in Table 3. The stress-strain plot of the hybrid sample together with the details of its sub-regions is presented in Fig. 9, along with the plots of the individual wrought and AM conditions (i.e. samples that were either only in wrought or AM condition).

Fig. 9 shows that the individual wrought condition had a lower yield stress (336 MPa) but a higher ultimate tensile stress (779 MPa) in comparison with the individual AM condition (448 MPa and 751 MPa, respectively). In other words, the wrought condition had a higher hardening rate than the AM condition. The difference in yield stresses is related to the difference in microstructure between the two conditions. Despite containing a larger grain size (Table 1 and Fig. 5), the AM condition had a much higher initial dislocation density than the wrought condition. The calculated average GND density in the AM condition before deformation (3.3×10^{13} m^{-2}) was nearly twice that of its wrought counterpart (1.6×10^{13} m^{-2}). This high initial dislocation density in the AM condition explains its initial yield stress. The DIC measurements, Fig. 9, show that the wrought and AM sides in the hybrid sample have a nearly identical tensile response to the respective individual wrought and AM conditions. However, the total strain of the

Table 2
Chemical measurement in mass percent using EDS.

	Ni (%)	Fe (%)	Mn (%)	Cr (%)	Mo (%)	Nb (%)	Ti (%)	Cu (%)	C (%)	Al (%)
Precipitates in wrought region	1.81 ± 1.30	1.48 ± 1.27	0.30 ± 0.41	0.72 ± 0.79	3.26 ± 1.32	66.11 ± 2.52	7.35 ± 1.26	0.41 ± 0.85	17.13 ± 1.42	0.52 ± 0.43

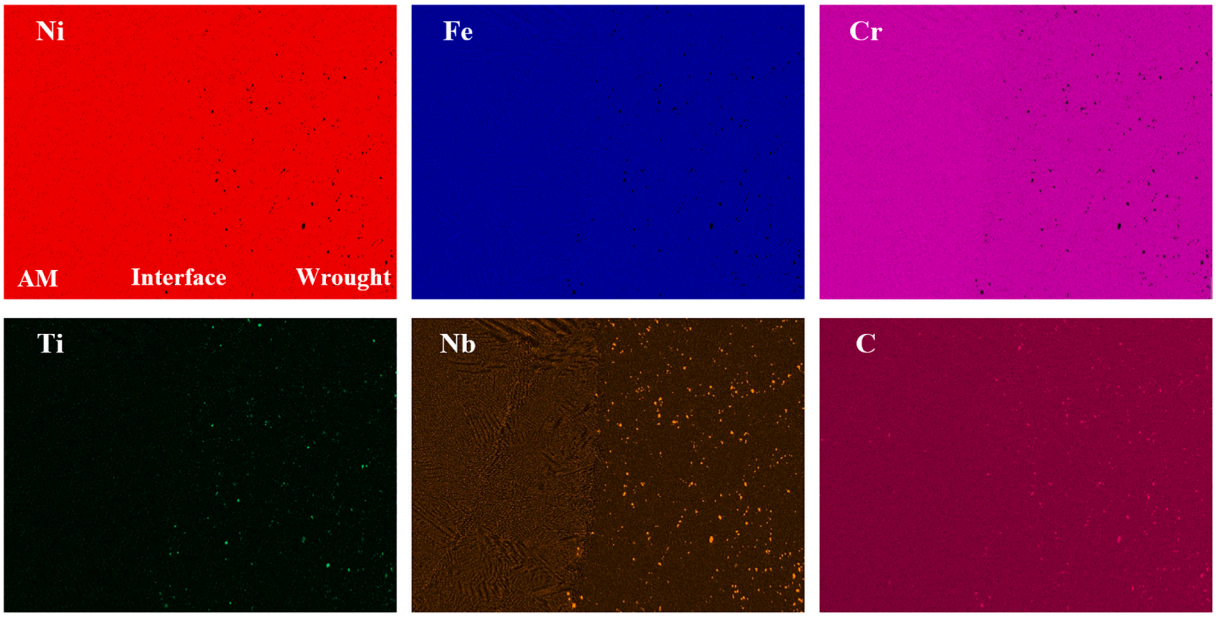

Fig. 7. Elemental maps in the bond interface region and its surroundings.

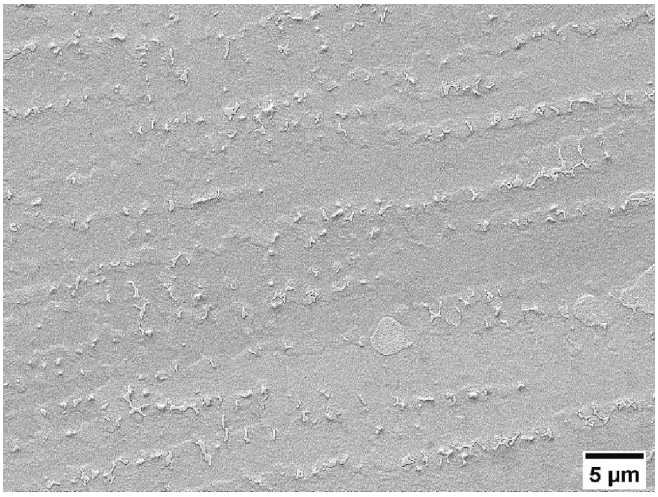

Fig. 8. Laves phase in the interdendritic regions in the AM microstructure.

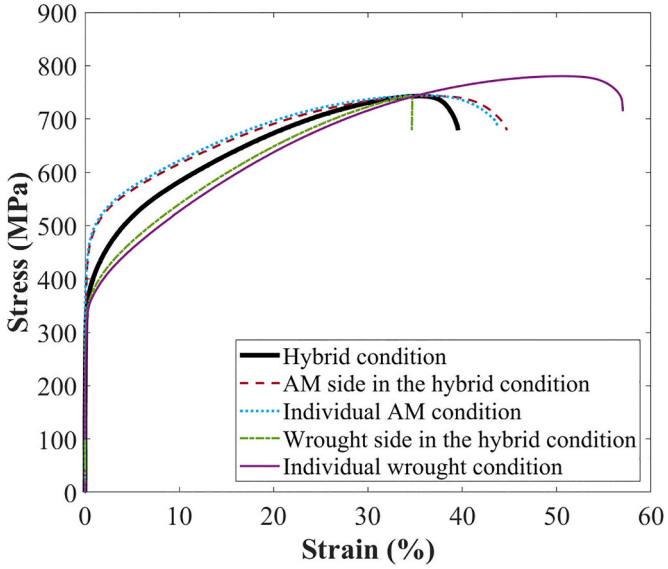

Fig. 9. Representative stress-strain curves of hybrid sample with its sub-regions in addition to the individual wrought and AM conditions.

Table 3
Tensile properties.

	Yield stress (MPa)	Ultimate tensile stress (MPa)	Total elongation (%)
Hybrid samples	311 ± 48	725 ± 18	37 ± 2
AM region in a hybrid sample	434	–	44
Wrought region in a hybrid sample	345	–	34
AM condition	448 ± 2	751 ± 7	42 ± 2
Wrought condition	336 ± 1	779 ± 1	56 ± 1

wrought side in the hybrid sample was lower than that of the individual wrought condition, suggesting that the wrought side in the hybrid condition should be able to accommodate further deformation should the sample not have failed prematurely. Most importantly, despite having a higher yield stress and good ductility, the AM side was the one in which localisation and fracture consistently occurred in the hybrid component.

DIC observations (Fig. 10) provided insights into the evolution of plastic deformation, in particular the development of localisation. Under the external load, the wrought region plastically deformed first while the AM side largely did not yield (Fig. 10a) because of the lower initial yield strength associated with the lower initial dislocation density in the wrought region (Table 3 and Fig. 4). As plastic deformation continued, the wrought side work-hardened because of the generation of dislocations during plasticity and the interactions between dislocations themselves and with other microstructure such as the grain boundaries and precipitates in the wrought region. The work-hardening of the wrought side increased its yield strength, reaching the same initial strength of the AM side, causing the AM side to plastically deform (Fig. 10a-b). The development of plasticity in the AM side diffused the plasticity (i.e. reduced the risk of localisation) in the wrought side. The redistribution of plasticity between the AM and wrought sides is similar to the load shedding observed in a combination of hard and soft grains [36,37].

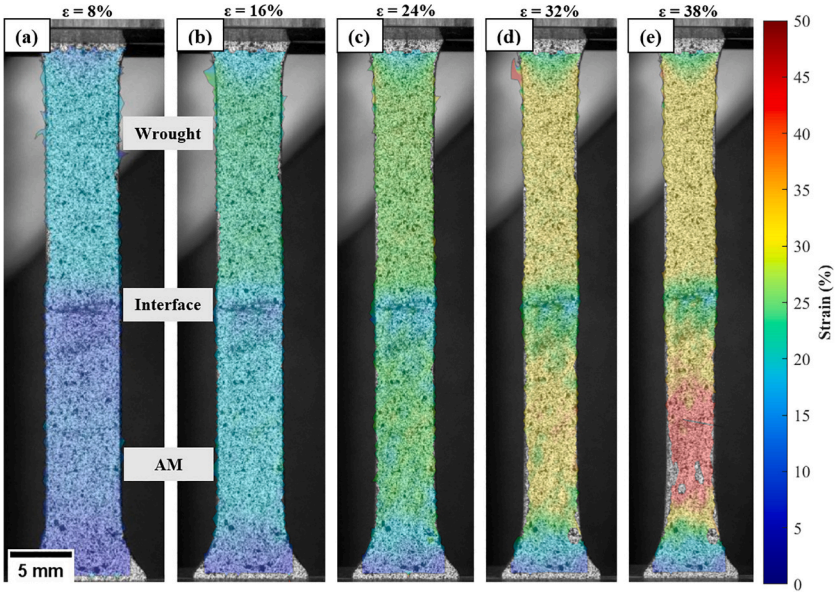

Fig. 10. (a-e) Deformation stages of the hybrid wrought-AM Inconel 718 under uniaxial loading. The global strain at each stage is indicated at the top of every image. All figures have the same scale bar shown in (a).

Once the AM side started to yield, the further plastic inhomogeneity of the hybrid condition depended on the localisation resistance that is strongly dependent on the work-hardening rate – the higher the hardening rate the better the resistance to localisation. In general, the local strain in the localised band is higher than the surroundings, resulting in higher strength in the localised region thanks to the work-hardening. In other words, the localised region becomes stronger than its surroundings, resulting in the redistribution of plasticity to the surrounding area and diffusing the localised strain. If a material has a low hardening rate, the redistribution is minimal, worsening the localisation.

The work-hardening of the wrought and AM conditions can be quantified using the Ludwik-Hollomon equation [38,39]:

$$\sigma = \sigma_Y + K\varepsilon^n \tag{2}$$

where σ is the instantaneous yield stress in MPa, σ_Y is the initial yield stress, K is a coefficient, ε is the true plastic strain, and n is the work-hardening exponent. From the tensile results, the Ludwik-Hollomon parameters of the individual wrought and AM conditions were, respectively, calculated as:

$$\sigma = 336 + 1822\varepsilon^{0.85} \tag{3}$$

$$\sigma = 447 + 1302\varepsilon^{0.71} \tag{4}$$

According to Considère's criterion [40], the higher work-hardening exponent n results in longer uniform strain before the onset of plastic instability, i.e. better resistance to localisation. The AM condition has a lower n, Eqs. (3) and (4), reaffirming the lower resistance to localisation in this condition. However, thanks to the higher hardening of the wrought side, its strength kept increasing at a higher rate, and became almost the same as that of the AM side at a global strain of 32%. Beyond this global strain, most of the plasticity was accommodated by the AM side (Fig. 10d-e). Upon further loading, the deformation in the AM side was highly inhomogeneous with an increasingly intensifying localisation. Towards the final stages of loading, the localisation in the AM side (Fig. 10e) led to crack initiation and subsequently final fracture in the AM side.

The highly inhomogeneous deformation and lower hardening rate in the AM region are due to the spatial variation of the microstructure, namely the crystallographic orientations, grain size and dislocation density. The wrought side contained fine grains with a random distribution of crystallographic orientations (Table 1 and Fig. 5). The small grain size can induce higher strain-hardening according to the Hall-Petch relationship [41,42], partly explaining the higher hardening of the wrought side as shown in Table 4. The higher hardening rate, as explained, prevented the localisation in the wrought side. In addition, the uniform distribution of fine grains of random crystallographic orientations (i.e. uniform distribution of "soft" and "hard" grains) in the wrought side, Fig. 5h, promoted a more isotropic and homogeneous deformation, explaining the higher uniform strain (reflected by the coefficient n in Eq. (2)) for the wrought side. In comparison, the AM side contained much larger columnar grains (on the mm scale, Fig. 5g versus h), with few "soft" and "hard" grains occupying relatively large areas within the sample, as shown in the Taylor factor maps. The large grains induced a lower hardening rate during plastic deformation. The dislocation density was also already very high in the AM condition prior to deformation. Therefore, there was minimal generation of new dislocations during deformation while the annihilation of dislocations due to dynamic recovery should be high because of the high initial dislocation density, explaining the low hardening in the AM side. Localisation tends to develop in large grains with small Taylor factors (i.e. "soft" grains). The low hardening rate in the AM condition accelerated the strain localisation, increasing the plastic inhomogeneity in the AM side of the hybrid condition.

3.4.2. *Effect of the interface region*

The DIC results also reveal that the bond interface was the strongest region with the least plastic deformation throughout the uniaxial loading stages. In fact, none of the tested samples fractured in the

Table 4
Strain hardening rate of the individual wrought and AM conditions at a given global strain. Note "-"sign denotes an apparent softening. Such apparent softening seen in the AM side was due to the crack growth that occurred due to loss of load bearing area after the necking initiation.

Global strain ε (%)	Strain hardening rate in wrought condition (MPa)	Strain hardening rate in AM condition (MPa)
8	1365	955
16	1073	720
24	812	437
32	558	162
38	364	- 179

interface region. The local strain in the interface at the point of fracture was measured to be 20% and was nearly half the global strain of 40%. The strength of the interface is directly influenced by (1) the fine cellular dendritic microstructure (Fig. 4) that contained dense dislocations at the interdendritic regions in the AM side of the interface; and (2) the high dislocation density in the wrought side.

Vickers microhardness testing was performed on the polished surface of a hybrid sample, and the results are presented in Fig. 11. While the hardness of the wrought region was highest near the interface, the hardness of the AM region slightly varied towards the interface but was overall higher than that of the wrought side. The higher hardness in the region on the wrought side adjacent to the interface is due to the higher dislocation density, Fig. 4b. However, as the effect of heating and thermal gradient during the deposition diminished with increasing distance from the bond interface (in particular outside of the heat-affected zone), both the GNDs and the hardness level decreased and stabilised in regions that were about 2 mm away from the interface. It is worth noting that the hardness of the bulk AM region was higher than the wrought, in agreement with the higher initial strength measured from the uniaxial tension (Fig. 9), and this is also attributed to a high density of dislocations at interdendritic boundaries (including GNDs which were quantified to be twice as dense in the AM side in comparison with the wrought side, Fig. 6b).

3.5. Crack initiation mechanisms

As noted in the previous section, the failure of the hybrid condition consistently occurred in the AM side despite its good ductility and higher strength. This section examines the effect of the AM microstructure and plastic inhomogeneity development on the crack initiation. SEM imaging was performed on the fracture surfaces and gauge regions of the deformed hybrid wrought-AM Inconel 718 samples to reveal insights into the fracture mechanism. As shown in the micrograph in Fig. 12a-b, the cellular dendritic microstructure was clearly seen on the fracture surface, suggesting that the initiation and growth of cracks were related to the solidification microstructure. The surface also contained a significant number of dimples, which is indicative of a ductile fracture mode. Laves phase that is incoherent with the γ matrix in Inconel 718 [43,44] was observed in the fracture surface, suggesting the phase's involvement in the crack initiation.

As the plastic deformation progresses, dislocations increase along localised slip lines and pile up at hard obstacles which were the Laves phase in this study. Such pile-ups of dislocations at obstacles increase the internal stress in the front of the pile-ups, pushing the leading dislocations to shear through or creating new sources of dislocations in the front region. Fig. 12b and c show slip lines, suggesting dislocations sheared through Laves particles. As Laves particles are brittle, such shearing resulted in micro-cracking. Another mechanism of forming micro-cracks is related to the increased internal stress induced by the dislocation pile-ups. Micro-cracks can initiate in hard obstacles and often be aligned at about 70° to the slip lines as suggested by Stroh [45]. Such crack formation mechanism was seen in regions containing large Laves particles (the dashed rectangle in Fig. 12b that was magnified in Fig. 12d). Cracks were seen not to be aligned with the dislocation slip in the matrix, but inclined at an angle of 40° with respect to the slip lines, suggesting that such cracks were not due to the dislocation shearing. This angle was different to 70° that was theoretically predicted by Stroh probably due to the rotation of particles in the subsequent deformation. The increase in the internal stress at the interface between the matrix and Laves particle can also cause debonding at the interface, adding the third source of crack initiation. Fig. 12e and f show that micro-cracks coalesced to grow into larger cracks along the interdendritic regions. Such a development of cracks explains why the fracture surface contained a dendritic microstructure (Fig. 12a).

This study provides a direct observation demonstrating a key role in the fracture of Laves phase that acted as preferential sites for crack nucleation and propagation under the loading of DED Inconel 718. The detrimental impact of the Laves phase in Inconel 718 was reported previously in literature without detailed discussions on the underlying mechanisms [8,12,35,43,44,46]. However, this present study shows that the interaction between Laves phase and localised slip bands resulted in the formation of micro-cracks, causing an early crack initiation in DED Inconel 718. This effect is exacerbated by the low resistance to strain localisation due to a low hardening rate in the DED condition as discussed earlier in Section 3.4.1. The early initiation of cracks in the DED condition led to the observed reduced ductility of the hybrid Inconel 718 (Fig. 9). As the cellular dendritic features are also documented in Inconel 718 fabricated by other AM techniques [12,14,30,47–49], the insights presented in this study directly concerning the interplay between the precipitates, dislocations and crack initiation are also applicable to Inconel 718 fabricated by other AM methods. Engineering the microstructure to achieve fine grains (for example via achieving the columnar

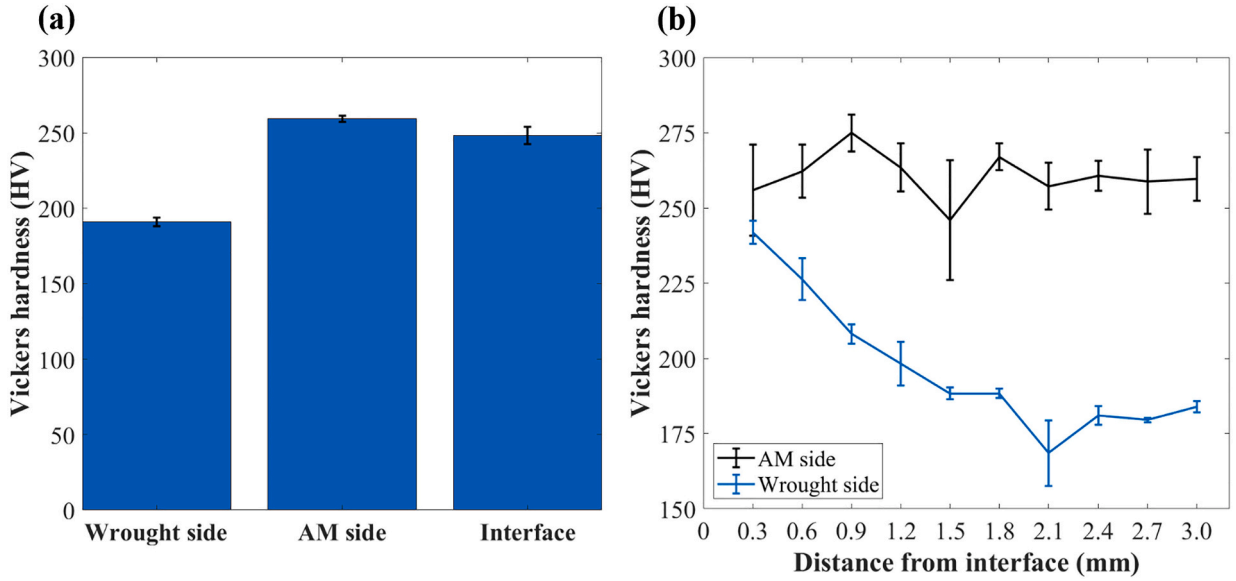

Fig. 11. Vickers microhardness testing results: (a) comparing the three regions in the hybrid Inconel 718; (b) outlining the local microhardness evolution with respect to distance from the bond interface.

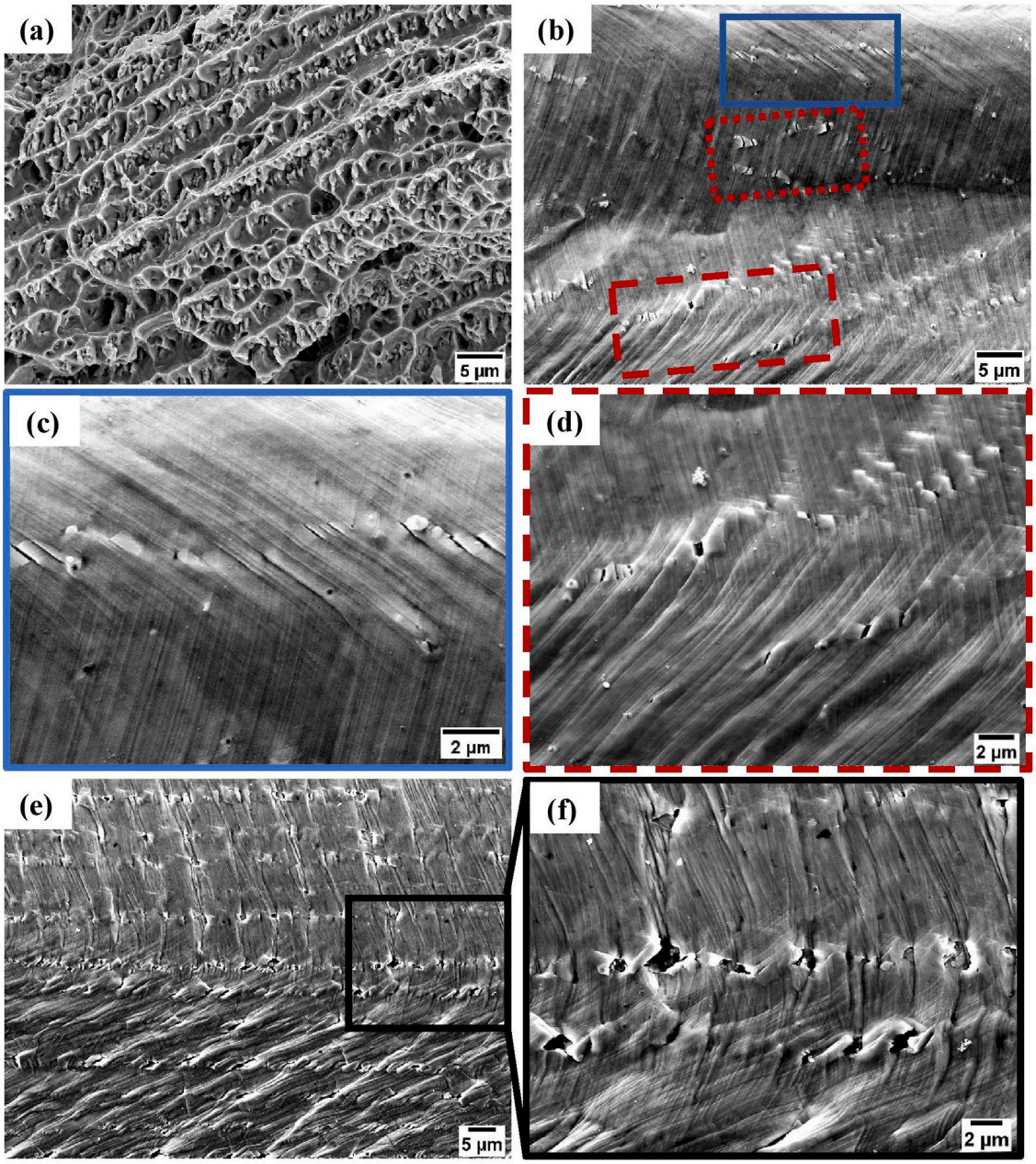

Fig. 12. Fracture surface of the DED Inconel 718: (a) cellular dendrites were seen on the fracture surface; (b) micro-cracks along the gauge region induced by shearing through fine particles and fracture of larger particles; (c) shearing-induced cracks in particles; (d) fracture of particles; (e) and (f) coalescence and growth of micro-cracks.

equiaxed transition in solidification), lowering the initial dislocation density in the as-built and the removal of the detrimental Laves phase via heat treatments should be a priority in improving the ductility of AM-processed Inconel 718.

4. Conclusions

This study presents the constitutive relationship between the local microstructure and the spatial deformation response of hybrid wrought-AM Inconel 718, and reveals the origins of the strength of the bond interface. The study also sheds light on the role of the local microstructure (grain crystallographic orientations, grain size, initial dislocation density/distribution and Laves) in the development of plastic inhomogeneity, in particular localised slip bands, and how Laves phase interacts with the localised slip bands to result in the early crack initiation in the hybrid condition, impacting the mechanical integrity and compromising the ductility. The main findings are:

(1) Hybrid wrought-AM Inconel 718 components were fabricated successfully with excellent consolidation and very minimal porosity.
(2) DIC analysis revealed that the bond interface is the strongest region in the hybrid sample due to (1) small grains with a high dislocation density and fine cellular dendrites in the AM side of the interface, and (2) a high dislocation density in the wrought side of the interface.
(3) Although the AM side had a higher initial yield strength (hence higher hardness) thanks to higher initial dislocation density in comparison to the wrought side, severe plastic inhomogeneity (in particular severe localisation) was observed in the AM side. The

inhomogeneity was primarily attributed to low hardening induced by very few, but large grains of preferential orientations for slip, and low generation rate of dislocations during deformation. On the contrary, the fine and randomly oriented grain microstructure in the wrought region led to a homogeneous deformation with a higher hardening rate that prevented the strain localisation.

(4) This present study reveals the main mechanism responsible for the failure in additively manufactured Inconel 718. Plastic inhomogeneity causes strain localisation in the AM region. The interactions between the localised slip and brittle Laves phase in the AM region are the main mechanism for crack initiation, which subsequently led to final fracture. The mechanical integrity of hybrid Inconel 718 can be improved by achieving more equiaxed and randomly oriented grains (e.g., by changing the scanning strategy and controlling the solidification mode), lowering dislocation densities and minimising the Laves phase content through heat treatments.

Declaration of Competing Interest

The authors declare that they have no known competing financial interests or personal relationships that could have appeared to influence the work reported in this paper.

Data availability

The raw/processed data required to reproduce these findings cannot be shared at this time as the data also forms part of an ongoing study.

Acknowledgments

J. Al-Lami would like to thank Richard Cross, Edward Cross and Aidan Bew at Cross Manufacturing Company for supporting this work. The assistance of Dr. Hang Xu with DIC tensile testing is also acknowledged and appreciated.

References

[1] T. DebRoy, T. Mukherjee, H.L. Wei, J.W. Elmer, J.O. Milewski, Metallurgy, mechanistic models and machine learning in metal printing, Nat. Rev. Mater. 6 (2021) 48–68, https://doi.org/10.1038/s41578-020-00236-1.

[2] B. Onuike, A. Bandyopadhyay, Additive manufacturing in repair: influence of processing parameters on properties of Inconel 718, Mater. Lett. 252 (2019) 256–259, https://doi.org/10.1016/j.matlet.2019.05.114.

[3] B. Graf, A. Gumenyuk, M. Rethmeier, Laser metal deposition as repair technology for stainless steel and titanium alloys, Phys. Procedia 39 (2012) 376–381, https://doi.org/10.1016/j.phpro.2012.10.051.

[4] J.H. Yu, Y.S. Choi, D.S. Shim, S.H. Park, Repairing casting part using laser assisted additive metal-layer deposition and its mechanical properties, Opt. Laser Technol. 106 (2018) 87–93, https://doi.org/10.1016/j.optlastec.2018.04.007.

[5] I. Kelbassa, P. Albus, J. Dietrich, J. Wilkes, Manufacture and repair of aero engine components using laser technology, in: Proc. 3rd Pacific Int. Conf. Appl. Lasers Opt, Laser Institute of America, 2008, pp. 208–213, https://doi.org/10.2351/1.5057008.

[6] K. Richter, S. Orban, S. Nowotny, Laser cladding of the titanium alloy TI6242 to restore damaged blades, in: Proc. 23rd Int. Congr. Appl, Lasers Electro-Optics, Laser Institute of America, 2004, https://doi.org/10.2351/1.5060222.

[7] F. Soffel, D. Eisenbarth, E. Hosseini, K. Wegener, Interface strength and mechanical properties of Inconel 718 processed sequentially by casting, milling, and direct metal deposition, J. Mater. Process. Technol. 291 (2021), 117021, https://doi.org/10.1016/j.jmatprotec.2020.117021.

[8] M. Godec, S. Malej, D. Feizpour, M. Donik, D. Balažic, L. Klobčar, M. Pambaguian, A. Kocijan Conradi, Hybrid additive manufacturing of Inconel 718 for future space applications, Mater. Charact. 172 (2021), https://doi.org/10.1016/j.matchar.2020.110842.

[9] Y.C. Yeoh, G. Macchi, E. Jain, B. Gaskey, S. Raman, G. Tay, D. Verdi, A. Patran, A. M. Grande, M. Seita, Multiscale microstructural heterogeneity and mechanical property scatter in Inconel 718 produced by directed energy deposition, J. Alloys Compd. 887 (2021), 161426, https://doi.org/10.1016/j.jallcom.2021.161426.

[10] C. Guévenoux, S. Hallais, Y. Balit, A. Charles, E. Charkaluk, A. Constantinescu, Plastic strain localization induced by microstructural gradient in laser cladding repaired structures, Theor. Appl. Fract. Mech. 107 (2020), https://doi.org/10.1016/j.tafmec.2020.102520.

[11] Z. Zhao, J. Chen, Q. Zhang, H. Tan, X. Lin, W. Dong Huang, Microstructure and mechanical properties of laser additive repaired Ti17 titanium alloy, Trans. Nonferrous Metals Soc. China 27 (2017) 2613–2621, https://doi.org/10.1016/S1003-6326(17)60289-9. English Ed.

[12] H. Qi, M. Azer, A. Ritter, Studies of standard heat treatment effects on microstructure and mechanical properties of laser net shape manufactured Inconel 718, Metall. Mater. Trans. A. 40 (2009) 2410–2422, https://doi.org/10.1007/s11661-009-9949-3.

[13] L.L. Parimi, M.M. Attallah, J.C. Gebelin, R.C. Reed, Direct laser fabrication of Inconel-718 : Effects on distortion and microstructure, in: 12th Int. Symp. Superalloys, Seven Springs, PA, 2012, pp. 511–519.

[14] L.L. Parimi, G. Ravi, D. Clark, M.M. Attallah, Microstructural and texture development in direct laser fabricated IN718, Mater. Charact. 89 (2014) 102–111, https://doi.org/10.1016/j.matchar.2013.12.012.

[15] E. Hosseini, V.A. Popovich, A review of mechanical properties of additively manufactured Inconel 718, Addit. Manuf. 30 (2019), 100877, https://doi.org/10.1016/j.addma.2019.100877.

[16] Y. Balit, C. Guévenoux, A. Tanguy, M.V. Upadhyay, E. Charkaluk, A. Constantinescu, High resolution digital image correlation for microstructural strain analysis of a stainless steel repaired by directed energy deposition, Mater. Lett. 270 (2020), 127632, https://doi.org/10.1016/j.matlet.2020.127632.

[17] S. Birosca, G. Liu, R. Ding, J. Jiang, T. Simm, C. Deen, M. Whittaker, The dislocation behaviour and GND development in a nickel based superalloy during creep, Int. J. Plast. 118 (2019) 252–268, https://doi.org/10.1016/J.IJPLAS.2019.02.015.

[18] D.P. Field, P.B. Trivedi, S.I. Wright, M. Kumar, Analysis of local orientation gradients in deformed single crystals, Ultramicroscopy. 103 (2005) 33–39, https://doi.org/10.1016/j.ultramic.2004.11.016.

[19] W. Pantleon, Resolving the geometrically necessary dislocation content by conventional electron backscattering diffraction, Scr. Mater. 58 (2008) 994–997, https://doi.org/10.1016/j.scriptamat.2008.01.050.

[20] M. Jin, E. Hosseini, S.R. Holdsworth, M.-S. Pham, Thermally activated dependence of fatigue behaviour of CrMnFeCoNi high entropy alloy fabricated by laser powder-bed fusion, Addit. Manuf. 51 (2022), 102600, https://doi.org/10.1016/j.addma.2022.102600.

[21] A. Piglione, B. Attard, V. Vieira, C.S. Maldonado, M.M. Attallah, S. Primig, M. Pham, On the constitutive relationship between solidification cells and the fatigue behaviour of IN718 fabricated by laser powder bed fusion, Addit. Manuf. 47 (2021), 102347, https://doi.org/10.1016/j.addma.2021.102347.

[22] Y.M. Wang, T. Voisin, J.T. McKeown, J. Ye, N.P. Calta, Z. Li, Z. Zeng, Y. Zhang, W. Chen, T.T. Roehling, R.T. Ott, M.K. Santala, P.J. Depond, M.J. Matthews, A. V. Hamza, T. Zhu, Additively manufactured hierarchical stainless steels with high strength and ductility, Nat. Mater. 17 (2018) 63–70, https://doi.org/10.1038/NMAT5021.

[23] Y. Chen, F. Lu, K. Zhang, P. Nie, S. Reza, E. Hosseini, K. Feng, Dendritic microstructure and hot cracking of laser additive manufactured Inconel 718 under improved base cooling, J. Alloys Compd. 670 (2016) 312–321, https://doi.org/10.1016/j.jallcom.2016.01.250.

[24] J.N. DuPont, C.V. Robino, A.R. Marder, M.R. Notis, Solidification of Nb-bearing Superalloys: part II. Pseudoternary solidification surfaces, Metall. Mater. Trans. A. 29 (1998) 2797–2806.

[25] S. Imbrogno, A. Alhuzaim, M.M. Attallah, Influence of the laser source pulsing frequency on the direct laser deposited Inconel 718 thin walls, J. Alloys Compd. 856 (2021), 158095, https://doi.org/10.1016/j.jallcom.2020.158095.

[26] B. Attard, S. Cruchley, C. Beetz, M. Megahed, Y.L. Chiu, M.M. Attallah, Microstructural control during laser powder fusion to create graded microstructure Ni-superalloy components, Addit. Manuf. 36 (2020), 101432, https://doi.org/10.1016/j.addma.2020.101432.

[27] S. Katayama, A. Matsunawa, Solidification microstructure of laser welded stainless steels, in: LIA (Laser Inst.) Am 43–48, 1985, pp. 60–67, https://doi.org/10.2351/1.5057623.

[28] T. DebRoy, H.L. Wei, J.S. Zuback, T. Mukherjee, J.W. Elmer, J.O. Milewski, A. M. Beese, A. Wilson-Heid, A. De, W. Zhang, Additive manufacturing of metallic components – process, structure and properties, Prog. Mater. Sci. 92 (2018) 112–224, https://doi.org/10.1016/j.pmatsci.2017.10.001.

[29] T.G. Gallmeyer, S. Moorthy, B.B. Kappes, M.J. Mills, B. Amin-Ahmadi, A. P. Stebner, Knowledge of process-structure-property relationships to engineer better heat treatments for laser powder bed fusion additive manufactured Inconel 718, Addit. Manuf. 31 (2020), 100977, https://doi.org/10.1016/j.addma.2019.100977.

[30] D. Zhang, W. Niu, X. Cao, Z. Liu, Effect of standard heat treatment on the microstructure and mechanical properties of selective laser melting manufactured Inconel 718 superalloy, Mater. Sci. Eng. A 644 (2015) 32–40, https://doi.org/10.1016/j.msea.2015.06.021.

[31] H. Xiao, S.M. Li, W.J. Xiao, Y.Q. Li, L.M. Cha, J. Mazumder, L.J. Song, Effects of laser modes on Nb segregation and laves phase formation during laser additive manufacturing of nickel-based superalloy, Mater. Lett. 188 (2017) 260–262, https://doi.org/10.1016/j.matlet.2016.10.118.

[32] Y. Chen, Y. Guo, M. Xu, C. Ma, Q. Zhang, L. Wang, Study on the element segregation and laves phase formation in the laser metal deposited IN718 superalloy by flat top laser and gaussian distribution laser, Mater. Sci. Eng. A 754 (2019) 339–347, https://doi.org/10.1016/j.msea.2019.03.096.

[33] M. Ma, Z. Wang, X. Zeng, Effect of energy input on microstructural evolution of direct laser fabricated IN718 alloy, Mater. Charact. 106 (2015) 420–427, https://doi.org/10.1016/j.matchar.2015.06.027.

[34] C. Zhong, A. Gasser, J. Kittel, K. Wissenbach, R. Poprawe, Improvement of material performance of Inconel 718 formed by high deposition-rate laser metal deposition, Mater. Des. 98 (2016) 128–134, https://doi.org/10.1016/j.matdes.2016.03.006.
[35] Z. Li, J. Chen, S. Sui, C. Zhong, X. Lu, X. Lin, The microstructure evolution and tensile properties of Inconel 718 fabricated by high-deposition-rate laser directed energy deposition, Addit. Manuf. 31 (2020), 100941, https://doi.org/10.1016/j.addma.2019.100941.
[36] V. Hasija, S. Ghosh, M.J. Mills, D.S. Joseph, Deformation and Creep Modeling in Polycrystalline Ti – 6Al Alloys 51, 2003, pp. 4533–4549, https://doi.org/10.1016/S1359-6454(03)00289-1.
[37] F.P.E. Dunne, D. Rugg, On the mechanisms of fatigue facet nucleation in titanium alloys, Fatigue Fract. Eng. Mater. Struct. (2008) 949–958, https://doi.org/10.1111/j.1460-2695.2008.01284.x.
[38] P. Ludwik, Elemente der technologischen Mechanik, Springer, 1909.
[39] J.H. Hollomon, Tensile deformation, Trans. Metall. Soc. AIME 162 (1945) 268–290.
[40] A. Considère, Mémoire sur l'emploi du fer et de l'acier dans les constructions, Ann. Des Ponts Chaussées 9 (1885) 574–775.
[41] E.O. Hall, The deformation and ageing of mild steel: III discussion of results, Proc. Phys. Soc. Sect. B. 64 (1951) 747–753, https://doi.org/10.1088/0370-1301/64/9/303.
[42] N.J. Petch, The cleavage strength of polycrystals, J. Iron Steel Inst. 174 (1953) 25–28.
[43] A. Bansal, A.K. Sharma, S. Das, P. Kumar, On microstructure and strength properties of microwave welded Inconel 718/stainless steel (SS-316L), Proc. Inst. Mech. Eng. Part L J. Mater. Des. Appl. 230 (2016) 939–948, https://doi.org/10.1177/1464420715589206.
[44] T. Sonar, S. Malarvizhi, V. Balasubramanian, Influence of arc constriction current (ACC) on microstructural evolution and tensile properties of tungsten inert gas welded thin sheets of aerospace alloy, Aust. J. Mech. Eng. 00 (2020) 1–20, https://doi.org/10.1080/14484846.2020.1794512.
[45] A.N. Stroh, The formation of cracks as a result of plastic flow, Proc. R. Soc. Lond. Ser. A. Math. Phys. Sci. 223 (1954) 404–414, https://doi.org/10.1098/rspa.1954.0124.
[46] S. Sui, J. Chen, R. Zhang, X. Ming, F. Liu, X. Lin, The tensile deformation behavior of laser repaired Inconel 718 with a non-uniform microstructure, Mater. Sci. Eng. A 688 (2017) 480–487, https://doi.org/10.1016/j.msea.2017.01.110.
[47] A. Alhuzaim, S. Imbrogno, M.M. Attallah, Controlling microstructural and mechanical properties of direct laser deposited Inconel 718 via laser power, J. Alloys Compd. 872 (2021), 159588, https://doi.org/10.1016/j.jallcom.2021.159588.
[48] L. Zhou, A. Mehta, B. Mcwilliams, K. Cho, Y. Sohn, Microstructure, precipitates and mechanical properties of powder bed fused inconel 718 before and after heat treatment, J. Mater. Sci. Technol. 35 (2019) 1153–1164, https://doi.org/10.1016/j.jmst.2018.12.006.
[49] E. Chlebus, K. Gruber, B. Ku, J. Kurzac, T. Kurzynowski, Effect of heat treatment on the microstructure and mechanical properties of Inconel 718 processed by selective laser melting, Mater. Sci. Eng. A 639 (2015) 647–655, https://doi.org/10.1016/j.msea.2015.05.035.